Electronic and magnetic phase diagrams of the Kitaev quantum spin liquid candidate $Na_2Co_2TeO_6$

Shengzhi Zhang,[1,*] Sangyun Lee,[2] Andrew J. Woods,[2] William K. Peria,[1] Sean M. Thomas,[2] Roman Movshovich,[2] Eric Brosha,[3] Qing Huang,[4] Haidong Zhou,[4] Vivien S. Zapf,[1,†] and Minseong Lee[1,‡]

[1]*National High Magnetic Field Laboratory, Los Alamos National Laboratory, Los Alamos, New Mexico 87545, USA*

[2]*MPA-Q, Los Alamos National Laboratory, Los Alamos, New Mexico 87545, USA*

[3]*Los Alamos National Laboratory, Los Alamos, New Mexico 87545, USA*

[4]*Department of Physics, University of Tennessee, Knoxville, Tennessee 37996, USA*

(Received 17 January 2023; revised 14 June 2023; accepted 17 July 2023; published 17 August 2023)

The $3d^7$ Co^{2+}-based insulating magnet $Na_2Co_2TeO_6$ has recently been reported to have strong Kitaev interactions on a honeycomb lattice and is thus being considered as a Kitaev quantum spin liquid candidate. However, due to the existence of other types of interactions, a spontaneous long-range magnetic order occurs. This order is suppressed by applied magnetic fields leading to a succession of phases and ultimately saturation of the magnetic moments. The precise phase diagram, the nature of the phases, and the possibility that one of the field-induced phases is a Kitaev quantum spin liquid phase are still a matter of debate. Here we measured an extensive set of physical properties to build the complete temperature-field phase diagrams to magnetic saturation at 10 T for magnetic fields along the a and a^* axes, and a partial phase diagram up to 60 T along c. We probe the phases using magnetization, specific heat, magnetocaloric effect, magnetostriction, dielectric constant, and electric polarization, which is a symmetry-sensitive probe. With these measurements, we identify all the previously incomplete phase boundaries and find additional high-field phase boundaries. We find strong magnetoelectric coupling in the dielectric constant and moderate magnetostrictive coupling at several phase boundaries. Furthermore, we detect the symmetry of the magnetic order using electrical polarization measurements under magnetic fields. Based on our analysis, the absence of electric polarization under zero or finite magnetic field in any of the phases or after any combination of magnetic/electric field cooling suggests that a zigzag spin structure is more likely than a triple-Q spin structure at zero field. Finally, we investigate the hysteresis and first- or second-order nature of each phase transition and its entropy changes. With this information, we establish a map of the magnetic phases of this compound and its magnetic, thermodynamic, and magnetoelectric properties, and discuss where spin liquid or other phases may be sought in future studies.

DOI: 10.1103/PhysRevB.108.064421

I. INTRODUCTION

Magnetism on a honeycomb lattice with antiferromagnetic nearest-neighbor *isotropic* exchange interactions is not frustrated. However, when the exchange interactions are dominated by *bond-dependent* Kitaev interactions, strong magnetic frustration results and the intriguing Kitaev quantum spin liquid (KQSL) is predicted to form as the ground state [1]. The Kitaev exchange interaction is of the form $K_x S_i^x S_j^x$, $K_y S_i^y S_j^y$, and $K_z S_i^z S_j^z$, representing the three types of bonds in a honeycomb lattice.

KQSLs are of particular interest to the quantum computing community because they host non-Abelian anyonic excitations in applied magnetic fields [1]. Non-Abelian anyons change the observable state of the system if they are braided (moved around each other) and these braiding operations have been shown to be capable of supporting fault-tolerant quantum computations [1,2]. However, the discovery of KQSLs in real magnets is still a significant challenge. KQSL candidate materials show both Kitaev and Heisenberg interactions, as well as other terms like off-diagonal exchange interactions and single-ion anisotropies. Thus, most known candidates form static long-range magnetic order at zero magnetic field (see below). Luckily, it has been predicted that if the non-Kitaev interactions are small enough, the long-range order can be suppressed by magnetic field in favor of a KQSL state [3,4].

The Kitaev interaction can be realized at a certain balance of crystal field and spin-orbit coupling with 90° exchange paths. With octahedral crystal fields, orbitals split into e_g and t_{2g} levels. Five electrons residing in t_{2g} lead to total $S = 1/2$ and $L = 1$. The strong spin-orbit coupling mixes S and L to form a spin-orbit entangled $j_{\text{eff}} = \frac{1}{2}$ Kramers' doublet, whose narrow band opens a Mott gap. The conventional Heisenberg-type exchange interactions are suppressed due to quantum interference between multiple paths across ligand ions on edge-sharing octahedra [5].

Due to the need for strong spin-orbit coupling, most research on potential KQSLs has focused on $4d$ and $5d$ ions with the low-spin d^5 electron configuration such as Ru^{3+} and Ir^{4+}. The first prominent candidates were honeycomb iridium oxides A_2IrO_3 with A = Na, Li [6], which have recently

*shengzhi@lanl.gov
†vzapf@lanl.gov
‡ml10k@lanl.gov

 ©2023 American Physical Society

been extended to include $A_3LiIr_2O_6$ with $A =$ Ag and H [7–9]. All these candidates except for $H_3LiIr_2O_6$ show magnetic ordering at zero magnetic field while $Ag_3LiIr_2O_6$ was shown to form magnetic ordering in less disordered crystals [10,11] and may show a KQSL in applied magnetic fields. Another highly promising candidate is α-$RuCl_3$ [12]. It exhibits continuum spin excitations in neutron scattering experiments [13,14] around the Brillouin zone center, which signifies flux excitations in addition to the itinerant Majorana fermions. Moreover, albeit seemingly dependent on growth techniques, the precise stacking structure, and phonon contributions, a potential half-quantized thermal Hall conductivity suggests a chiral quantum spin liquid phase stabilized by magnetic fields [3,4,15–17].

More recently, it has been proposed that certain $3d$ transition metals, which were previously dismissed by the conventional wisdom that they have small spin-orbit coupling, can also host the Kitaev exchange interactions playing a dominant role in their magnetism [18–20]. It is noted that as long as the spin-orbit coupling is comparable to or larger than the exchange and orbital-lattice interactions, the Kitaev interaction can still dominate. Indeed, d^7 Co^{2+} with the high spin configuration $t_{2g}^5 e_g^2$ has been shown to provide a strongly spin-orbit entangled $j_{\text{eff}} = 1/2$ degree of freedom with Kitaev interactions [18–20]. In $3d^7$ systems, the Kitaev interaction comes almost entirely from the t_{2g}-e_g hopping process. It is calculated to dominate over the Heisenberg interactions because the e_g-e_g Heisenberg and off-diagonal exchange interactions cancel those from the t_{2g}-e_g hopping process [20]. In addition, it is helpful that the more localized nature of $3d$ orbitals compared to $4d$ or $5d$ helps suppress longer-range exchange interactions [18–20].

$Na_2Co_2TeO_6$ has been proposed as a candidate $3d$ KQSL compound due to its honeycomb lattice and the observation in inelastic neutron scattering studies of Kitaev interactions [21–24]. Co^{2+} has a $3d^7$ electronic configurations under octahedral crystal field and Co^{2+}–O^{2-}–Co^{2+} form close to 90° bonds with spin-orbit coupling comparable to other energy scales [25]. Such nearly ideal oxygen octahedron geometry [25] helps suppress Heisenberg and symmetric off-diagonal terms [20]. Some calculations predict a ferromagnetic Kitaev interaction [18,19] while the inelastic neutron scattering measurements [21–24] support dominant antiferromagnetic Kitaev exchange. A theory by Winter considered both possibilities, and finds Kitaev interactions to be small compared to a third-nearest neighbor Heisenberg interaction via the Te atom in the center of the plaquette [26].

The space group of $Na_2Co_2TeO_6$ is $P6_322$ (No. 182). The magnetic honeycomb layers of Co^{2+} are separated by nonmagnetic Na^+ layers, which makes $Na_2Co_2TeO_6$ a magnetically quasi-two-dimensional system [25]. In comparison to α-$RuCl_3$, $Na_2Co_2TeO_6$ is structurally more robust and no other stacking sequence of layers has been detected [27].

To explore the ground state and its evolution under magnetic field, several phase diagrams were constructed in the literature [22,28–30]. However, these studies do not all extend to magnetic saturation and certain phase boundaries still need closer investigation as they may surround a KQSL phase. Furthermore, although the ground state at low temperature in zero field is well established to be antiferromagnetic [31], its spin structure is still under debate. A zigzag structure [31] similar to α-$RuCl_3$ [32] was initially proposed due to commonality observed in both systems [22]. The detected magnon dispersion from neutron diffraction can be well fitted using models based on the zigzag spin structure despite the discrepancies in fitting parameters among different studies [21,23,33,34]. However, more recent inelastic neutron scattering [35] and nuclear magnetic resonance studies [36] proposed a triple-Q order as the ground-state spin structure. We also note that due to slightly different environments of the two Co, a ferrimagnetic magnetization was observed [37].

Multiple phases are observed in $Na_2Co_2TeO_6$ with applied magnetic field. A phase emerging above 9.5 T is established as a mostly spin-polarized phase from magnetization and specific heat measurements [28,37]. However, the nature of other phases is still not determined. For instance, a phase is observed in single-crystalline $Na_2Co_2TeO_6$ above a metamagnetic phase transition at about 6 T. This phase mimics a putative KQSL phase in α-$RuCl_3$ in many aspects such as observations of a plateau in field-dependent magnetic entropy and of an additional electron spin resonance mode [22]. Therefore, it was also considered as a spin-disordered phase. However, because of the lack of enough data points, the phase boundaries are not well-defined and the nature of this phase is still not clear. Additionally, another phase was observed at between 8 T and saturation field in thermal conductivity measurement [28] and in a combined study using torque magnetometry and inelastic neutron scattering [30] measurements with magnetic field applied along the a^* axis. This phase, instead of the above mentioned, was recently proposed to be a KQSL phase [30], but this also needs further confirmation from other measurements. Thus, it is necessary to establish a more complete phase diagram from many different experimental techniques that reaches the full saturation of the magnetization to clarify the behaviors of this material.

In this paper, we construct comprehensive temperature-magnetic field (**T**-**H**) phase diagrams along both a and a^* axes based on the magnetic, thermodynamic, electric, and elastic properties of $Na_2Co_2TeO_6$. We also investigate a partial phase diagram for $\mathbf{H} \parallel c$. We observe a series of three phase transitions in magnetic fields for $\mathbf{H} \parallel a$ and a^*. Most previous papers saw only various subsets of these three phase transitions due to a limited number of measurement techniques, though recent torque magnetometry and inelastic neutron scattering data [30] show evidence of all three. For $\mathbf{H} \parallel a$, we also observe apparent phase transitions T_1 and T_2 as a function of temperature in the thermal expansion and specific heat at high fields that were not previous reported.

We do not observe temperature or field-dependent electric polarization onsetting at any of the magnetic phase boundaries in both single crystals along the a^* axis with $\mathbf{H} \parallel a$ axis and in a large polycrystal despite magnetic *and* electric poling. As will be explained in Sec. III, this disagrees with the triple-Q spin structure, which should produce an electric polarization under magnetic field. Rather, it favors the zigzag spin structure, whose symmetry does not support electric polarization with and without external magnetic fields. We note that in over 14 years of studying electric polarization at the National High Magnetic Field Laboratory in complex magnets, it was found that when the necessary symmetry conditions are

fulfilled, we always observe the expected electrical polarization in insulators. We also note that in $Na_2Co_2TeO_6$ we see strong coupling between magnetic and electric order parameters evidenced by magnetic-field- and temperature-dependent dielectric constants and peaks in the dielectric constant at some field-induced phase transitions (without concomitant peaks in the magnetostriction). Thus, the triple-Q ordering is not supported by our data. Therefore, either the zigzag or another spin structure that rules out linear magnetoelectric coupling is likely. At high fields for $\mathbf{H} \parallel a$ and a^*, we repeatedly observed additional phase transitions as a function of temperature in dilatometry and heat capacity. These may indicate subtle structural changes. Finally, when $\mathbf{H} \parallel c$ axis, five phases are observed in the $\mathbf{T} - \mathbf{H}$ phase diagram below 16 T as shown in Fig. S7 of the Supplemental Material (SM) [38] whereas the magnetization data became noisy at higher fields (Fig. S6 in the SM [38]) and it was hard to identify the critical fields. The temperature-dependent dielectric constant is shown to be independent of magnetic field and three broad humps are observed that do not match any of the magnetic transitions observed in magnetization measurements. As discussed in a later section, one possibility is that the dielectric humps are due to dynamics of different Na^+ configurations.

II. EXPERIMENTS

A. Crystal growth

The single crystals were grown by the flux method. A polycrystalline sample of $Na_2Co_2TeO_6$ was mixed with a flux of Na_2O and TeO_2 in a molar ratio of 1:0.5:2 and gradually heated to 900°C at 3°C/min in the air after grinding. The sample was kept at 900°C for 30 h and then was cooled to 500 °C/h at the rate of 3 °C/h. The furnace was then shut down to cool to room temperature. Crystal structure and purity were verified by x-ray diffraction and carefully oriented using a Laue x-ray diffractometer. Consistent magnetic susceptibilities of different single crystalline samples used in this paper confirm that all samples maintain the same crystal qualities and retain the same magnetic properties.

B. Magnetization and specific heat

Vibrating sample magnetometry (VSM) for dc magnetization, ac magnetic susceptibility, and specific heat measurements were performed in a 14 T Quantum Design Physical Property Measurement System (PPMS) using the built-in options with the magnetic field aligned along a and a^* axes.

Specific heat was obtained down to 1.9 K using the standard semiadiabatic heat pulse method in the PPMS. To align the field orientation, one edge of a single crystal sample was carefully adjusted and mounted on the stage of the PPMS vertical puck.

C. Electrical polarization, dielectric constant and electric field-induced magnetization

Electrical polarization measurements were performed by the standard technique of integrating the current as a function of time between the ground and the electrical contacts (two silver epoxy EPO-TEK H20E capacitor plates deposited on opposite sides of the sample) as the temperature or magnetic field changes. The areas of the electrodes for the a (a^*) direction were 0.28 mm^2 (1.11 mm^2) and the distance between the two electrodes was 0.46 mm (0.49 mm). Pt wires were used to electrically connect the electrodes on the samples to adjacent coaxial cables that, in turn, led to the room temperature electronics. These measurements were performed on both single and polycrystals in millisecond 65 T pulsed fields using a Stanford Research 570 current-to-voltage converter [39,40], and in a PPMS using a custom coaxial cable probe and a Keithley 6517A electrometer. The data shown in the main text were taken after electric poling, i.e., applying electric fields as described while cooling from high temperature through T_N to form an electric monodomain. We then measured the electric polarization both with and without applied electric and/or magnetic fields while sweeping the magnetic field as described in the SM [38].

On the same samples we also measured the electric capacitance as a function of magnetic field using an Andeen-Hagerling AH2700A capacitance bridge at 12 kHz and 15 V excitation with a custom-built co-axial cable probe in the PPMS. Temperature-dependent capacitance was measured at different frequencies using the same probe and samples but with an LCR Meter (Keysight E4980A).

Finally, we measured electric field-induced magnetization on the same polycrystals using the VSM in the PPMS, with a custom rod to apply electric field to the capacitor plates of the sample during measurement. The sample was poled by applying electric and magnetic fields of 2 kV/cm and 4 T, respectively, from 150 K. Electric field was then swept from −2 kV/cm to 2 kV/cm while measuring the magnetization.

D. Magnetocaloric effect

The magnetocaloric effect (sample temperature change versus magnetic field) measurement was performed in pulsed magnetic fields. In this measurement, a nearly adiabatic condition was realized due to the ultrafast field sweeping rate of $\sim$ 10 000 T/s. To obtain a strong thermal link between the sample and the thermometer on millisecond timescales in pulsed fields, a semiconducting 10-nm-thick AuGe thin film was directly deposited on the surface of the sample as a thermometer. The film was deposited by RF magnetron sputtering at 40 mTorr pressure of ultrahigh purity Ar gas for 60 min with 100 W power. Au contact pads were then deposited on top of the AuGe film with a shadow mask, leaving a stripe of AuGe uncovered. A custom digital lock-in method with 100 kHz source current was used to measure the thermometer resistance in pulsed fields, with four point contacts, as is usually employed at the NHMFL-PFF. A detailed picture of the setup can be found in the SM [38]. The thermometer was calibrated in thermalized conditions with exchange gas to obtain resistance versus temperature and an identical reference thermometer was used to obtain the magnetoresistance calibration.

E. Thermal expansion/magnetostriction

Length changes of the sample were measured as a function of temperature (thermal expansion) and magnetic field (magnetostriction). The Fiber Bragg Grating (FBG) dilatom-

etry measurement was adopted in the PPMS using a custom-built probe and optical fibers with 2 mm Bragg gratings [41]. A straight edge of the as-grown platelike single crystal of $Na_2Co_2TeO_6$ was carefully attached to the optical fiber using Henkel ultragel superglue. A Pt wire connected the sample to the Cernox temperature sensor, providing a proper thermal link between the two and to the bath. The FBG spectra were recorded using an optical sensing interrogator (Micron Optics, si155). The a- and a^*-axis data were recorded *in situ* with a third empty Bragg Grating as a reference to be subtracted from the sample signals [41]. The obtained thermal expansion as a function of magnetic field and temperature are normalized, respectively, following $\Delta L(H, T_0) = \Delta L(H, T_0)/\Delta L(0, T_0)$ and $\Delta L(H_0, T) = \Delta L(H_0, T)/\Delta L(H_0, 3.3\text{K})$. An illustration of the configuration of the sample attachment can be found in the SM [38]. To ensure reproducibility, two different pieces of samples were measured for each crystallographic orientation. To investigate possible effects of the superglue, one sample was measured twice for each orientation with regluing in between and found to be consistent.

III. SYMMETRY ANALYSIS TO DISTINGUISH ZIGZAG AND TRIPLE-Q

One of the major debates for $Na_2Co_2TeO_6$ is whether the ground-state magnetic ordering at zero magnetic field forms a zigzag [27] or a triple-Q [35] spin structure, as illustrated in Fig. 1(a). Here we show these two magnetic orderings can be distinguished using electric polarization measurements. Our results are consistent not with the triple-Q scenario but with the zigzag ordering or another non-polar magnetic ordering.

Electric polarization is a symmetry-sensitive measurement that detects the presence of a unique polar axis in the structure of the material. Linear magnetoelectric coupling is another symmetry-sensitive property, which detects the ability of a magnetic field to induce electric polarization or an electric field to induce magnetization with an odd coupling between them [42–44]. Linear magnetoelectric coupling is allowed in magnetic point groups that break time-reversal and spatial-inversion symmetry simultaneously at zero magnetic field. The field of multiferroics and magnetoelectrics has established over the past century that magnetic ordering influences the lattice and orbital configurations and so the magnetic symmetry can imprint itself on the lattice and create magnetoelectric coupling [42,45]. This magnetoelectric coupling occurs because every term in a magnetic Hamiltonian depends in some way on the underlying lattice symmetry. Thus, there is a back-coupling whereby the lattice deforms slightly to change the magnetic terms in the Hamiltonian and thereby lower the magnetic energy at the expense of the lattice deformation energy. Magnetostriction (with or without electric polarization) usually creates lattice constant changes on the order of 1 part in 10^3 to 10^5 in inorganic crystals [41]. Electric polarization can also result from rearrangement of electronic orbitals relative to their positively charged ions.

First, we note that $Na_2Co_2TeO_6$ is electrically insulating below 150 K, with a measured loss of 0.01 (0.03) nS at 3.3 (80) K, and thus no conduction electrons can screen an electric polarization. We show our measured magnetoelectric current ($I_p(H)$) as a function of pulsed magnetic field along the a^* axis

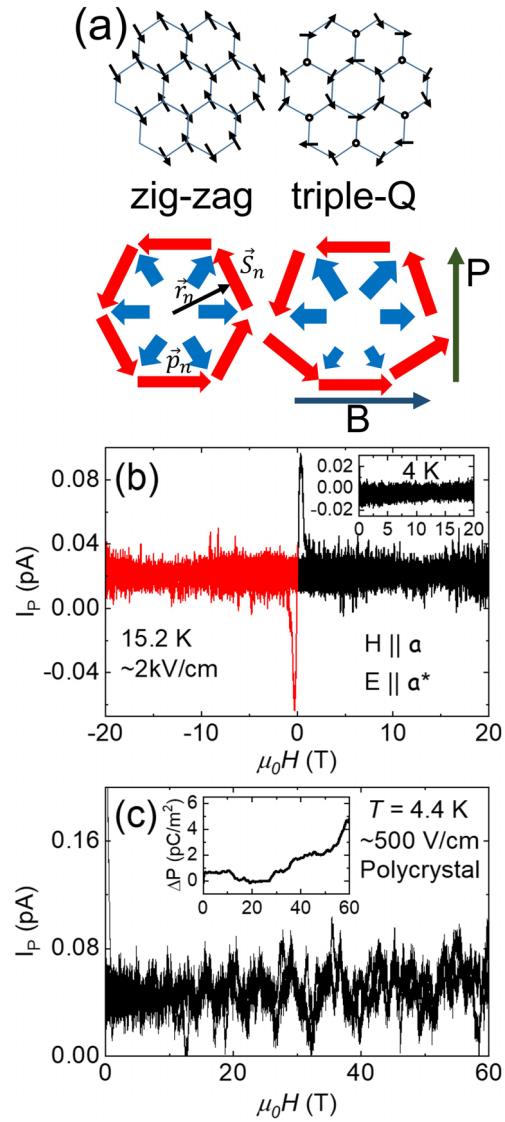

FIG. 1. (a) Top two panels illustrate the zigzag and triple-Q spin structures for phase I. Bottom two panels demonstrate the toroidal moment in the triple-Q structure (left) and how magnetic field induces a net electrical polarization (right). $\vec{S}_n$ and $\vec{r}_n$ are nth spin and the vector from the center of a toroidal moment to the nth spin, respectively. $\vec{p}_n$ are the electron dipoles. (b) Magnetoelectric current along a^* axis measured at 15.2 K with **H** ∥ **a** for both positive and negative field sweeps. The polling voltage is about 2 kV/cm. Inset depicts the positive sweep of the same measurement configuration at 4 K. (b) Magnetoelectric current of a polycrystal measured at 4.4 K with **H** ⊥ **E**. The poling voltage is about 500 V/cm. The inset shows the polarization of the same polycrystal.

with magnetic field along a axis at 15.2 K and 4 K in Fig. 1(b) and its inset, as well as on a polycrystal in Fig. 1(c) for **H** ⊥ **E**. The electric polarization of the polycrystal is shown in the inset of Fig. 1(c). These data were taken after cooling the sample in an electric field of 2 kV/cm (single crystal) and 500 V/cm (polycrystal) to align any polar domains. The magnetoelectric current is the derivative of the electric polarization with respect to time, and this current flows from the ground onto and off the capacitor plates (not through the sample) to compensate changes in the electric field within the sample. These data

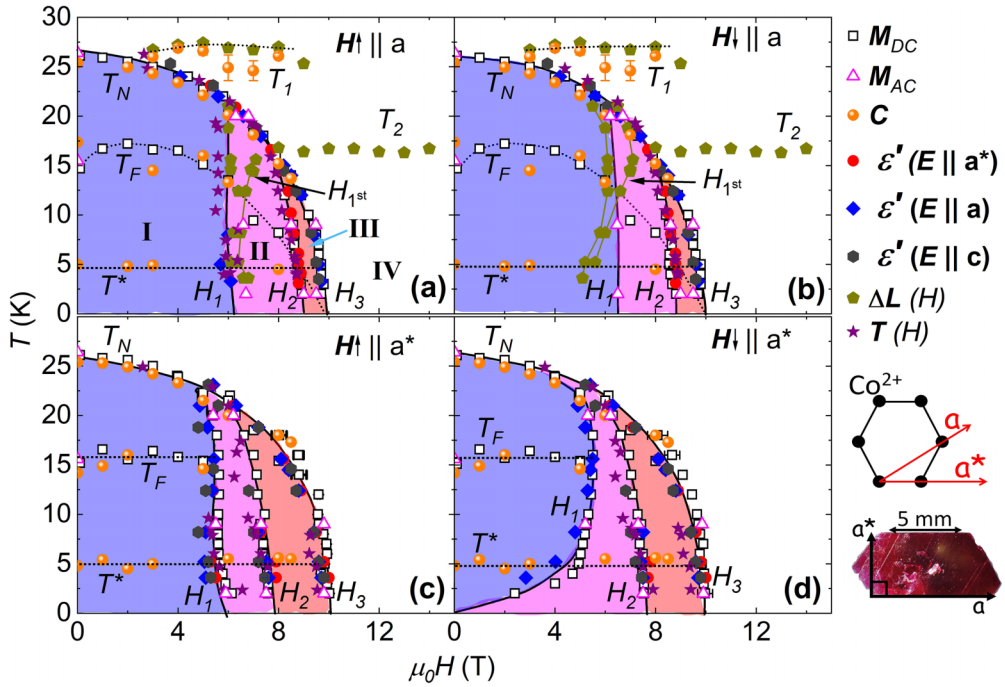

FIG. 2. Phase diagrams for $\mathbf{H} \parallel \mathbf{a}$ [(a), (b)] and $\mathbf{H} \parallel \mathbf{a}^*$ [(c), (d)] constructed from magnetization M, specific heat C, and dielectric constant ε' for three directions of the applied electric field $\mathbf{E}$ as indicated, magnetostriction $\Delta L(H)$, and magnetocaloric effect $T(H)$. $\mathbf{H}\uparrow$ and $\mathbf{H}\downarrow$ are the up- and downsweeps of the magnetic field, respectively. The solid or dotted lines are guides to the eyes. The hexagon in the legend defines the a and a^* axes with respect to the honeycomb lattice of Co^{2+}. At the bottom right is a photo of a single crystal with a and a^* axes indicated.

show no resolvable change in the electric polarization up to 60 T or at any of the field-induced phase transitions related to electric polarization in this compound. We note that due to fast magnetic field sweep rates up to ~ 10 kT/s, this measurement in pulsed fields is particularly sensitive—the signal to noise scales as the square root of the sweep rate. The observed peak at 0.3 T corresponds to a characteristic background noise at the beginning of the pulse and not to any phase transition observed by any other measurement in $Na_2Co_2TeO_6$. In the SM, we also show the same measurement as a function of temperature instead of magnetic field (pyroelectric current) after poling in an electric field. The data in Fig. S3 shows only drift and no electric polarization below 150 K [38]. Above 150 K, the data is affected by the onset of conductivity in the sample. These data were taken during the warming process after cooling the sample in an electric field of 2 kV/cm from 200 K, 150 K, 120 K, and 70 K as labeled in the figure.

We note that there is a report in the literature of ferroelectricity in $Na_2Co_2TeO_6$ below 60 K by Mukherjee *et al.* [46]. We do not find any ferroelectricity in our sample at this temperature. Also, the observation from Mukherjee *et al.* is inconsistent with space group $Na_2Co_2TeO_6$, which has been probed at low and high temperatures by various groups [25,27,47].

Now we discuss the expected electric polarization in the zigzag versus triple-Q spin structures for the low field phase denoted as phase I in Fig. 2. Combined with the crystal symmetry, the zigzag spin structure has a *magnetic point group* of $2221'$ (No. 6.2.18) with twofold rotational symmetry along all three directions, regardless of whether the ground state is purely antiferromagnetic or ferrimagnetic as reported in Ref. [37]. It forbids the spontaneous electric polarization. This point group has the magnetoelectric tensor $\alpha_{ij} = 0$, i.e., it also does not allow magnetic field-induced electric polarization. On the other hand, the triple-Q spin structure delineated in Ref. [35] breaks both inversion and time reversal symmetry. In particular, the triple-Q spin structure has non-zero off-diagonal components in $\boldsymbol{\alpha}$ within the plane ($\alpha_{12} = -\alpha_{21} \neq 0$) [48]. Hence, a linear magnetoelectric coupling is expected. That is, the electric polarization along a^* should emerge for magnetic fields along a and flip signs as the magnetic field sign is flipped. Below we demonstrate a detailed symmetry analysis. It is difficult to pinpoint the point group that the triple-Q spin structure possesses because no interlayer structure has been determined but our argument is valid as far as the net *toroidicity* defined below is nonzero.

In the triple-Q scenario [35], there exists a spontaneous toroidal moment as shown in Fig. 1(a). The order parameter $\vec{t}$ is defined as

$$\vec{t} = \sum_n (\vec{r}_n \times \vec{S}_n), \tag{1}$$

where $\vec{S}_n$ and $\vec{r}_n$ are nth spin and the vector from the center of a toroidal moment to the nth spin, respectively. $\vec{t}$ is odd both under spatial inversion and time-reversal operations, which allows the following form of the free energy [48]:

$$F(\mathbf{E}, \mathbf{H}) = F_0 - \frac{\varepsilon_{ij} E_i E_j}{8\pi} - \frac{\mu_{ij} H_i H_j}{8\pi} - \alpha_{ij} E_i H_j + \cdots, \tag{2}$$

where ε_{ij}, μ_{ij}, and α_{ij} are the dielectric permittivity, the magnetic permeability, and the magnetoelectric tensor, re-

spectively. Therefore, we expect the linearly increasing electric polarization as a function of the external magnetic field as follows:

$$P_i = \left(\frac{\varepsilon_{ij} - \delta_{ij}}{4\pi}\right) E_j + \alpha_{ij} H_j. \tag{3}$$

In our experiments, regardless of whether or not an electric field (E_i) is applied while sweeping the field (H_j) or while cooling from high temperatures, we observed no noticeable feature in the electric polarization versus magnetic field or temperature under all conditions as shown in Fig. 1 and Fig. S3 in the SM [38]. These measurements were repeated for single and polycrystals. In addition, we have also measured the electric field-induced magnetization, e.g., the converse magnetoelectric effect as shown in Fig. S3 in the SM [38] and no such effect is observed either. One possibility is that electric polarization is too small to be measured or that the lattice is too stiff to deform. We noted previously that both Zapf and Lee have never experienced such a scenario before. This scenario seems unlikely in the particular case of $Na_2Co_2TeO_6$ because, as shown in the next sections, we do observe both strong magnetodielectric effects (magnetocapacitance) and magnetostriction effects. Thus, we know that $Na_2Co_2TeO_6$'s lattice deforms in response to magnetic order and does form electric dipoles - just not a net electric polarization. The last possibility is that the electric polarization from different triple-Q planes cancel out. This possibility could also be excluded with the electric field poling that may align all toroidal moments along the out-of-plane direction if the interlayer coupling is small [35]. However, if the poling energy is not large enough to overcome the interlayer coupling strength, i.e., the interlayer coupling is very strong, then we cannot rule out this possibility.

Therefore, in the case where the interlayer coupling strength is not very strong, our data are not consistent with the magnetic structure of the triple-Q phase. They are consistent with the zigzag spin structure or with another spin structure that does not allow electric polarization under magnetic field. We notice that in a recently uploaded elastic neutron scattering study [49], a magnetic Bragg peak only recovered 2/3 of its intensity in the following field sweeps compared to the initial zero-field-cooled field sweep. This seems inconsistent with either triple-Q or zigzag structures. The inconsistency between our data and the neutron scattering study may be due to some differences in the samples, which seems unlikely because all critical temperatures and magnetic fields are consistent among the literature. Therefore, this may imply another exotic spin structure that could be consistent with both experiments.

IV. THE T-H PHASE DIAGRAM

A. Results

From the aforementioned various measurements, we constructed comprehensive $T - \mathbf{H}$ phase diagrams of $Na_2Co_2TeO_6$ as illustrated in Fig. 2 with field along the a and a^* axis. A phase diagram with $\mathbf{H} \parallel \mathbf{c}$ constructed from magnetization measurements can be found in the SM [38]. For clarity, we discuss an overview of the phase diagram before describing the details of the individual measurements below.

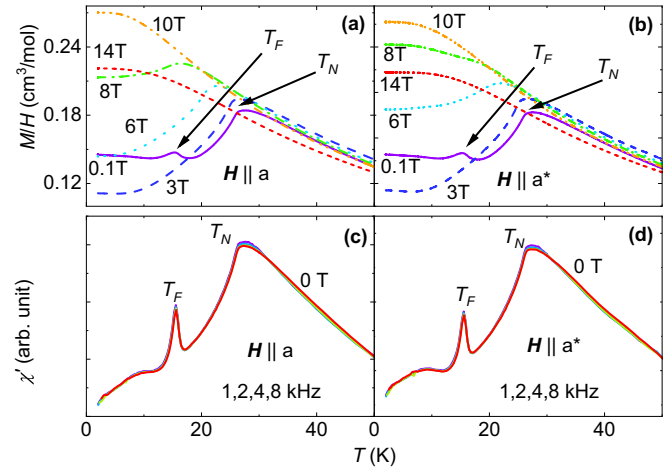

FIG. 3. Longitudinal dc magnetic susceptibility M/H vs T for various magnetic fields between 0.1 and 14 T along (a) a and (b) a^*. ac magnetic susceptibility χ' vs T for fields along the (c) a axis and (d) a^* axis. The ac field with amplitude 10 Oe is applied at 1,2,4,and 8 kHz with a dc field $H = 0$. T_F and T_N are the temperatures recorded in the phase diagram. The complete data sets are available in the SM [38].

From field-dependent measurements, there are four successive phases (I–IV), including the polarized phase, separated by the critical fields H_1, H_2, and H_3. As a function of temperature, three major phase boundaries are observed as T_N, T_F, and T^*, consistent with the literature [28,29,37]. We tracked T_F to higher fields than previously reported. It is noteworthy that the T_F boundary is qualitatively different when magnetic field is applied along a or a^* axes. It is field dependent and persists into phase II when magnetic field is applied along the a axis whereas it becomes field independent and stops within phase I when magnetic field is applied along the a^* axis. Several additional critical fields/temperatures (T_1, T_2, and H_{first}) were also observed in thermal expansion and specific heat measurements.

Figures 3(a) and 3(b) show the dc magnetic susceptibility (M/H) as a function of T taken at various magnetic fields H between 0.1 T and 14 T applied along a and a^*, respectively. T_N indicates the antiferromagnetic phase transition temperature ~27 K for both directions, consistent with other results [22,27,31,36,37,46]. Another peak around 16 K and at 0.1 T, denoted with T_F, is also observed for both directions. This feature has been interpreted as a signature of spin canting [22] and is the temperature at which a low-energy broad excitation spectra turn into a clear magnon band [35]. The peak at T_F is quickly suppressed as the applied magnetic field increases from 0.1 T to 1 T so its feature is only clearly visible in the derivatives at higher fields. On the other hand, T_N shifts towards lower temperatures and the feature becomes broadened with increasing field and eventually disappears above 8 T.

Figures 3(c) and 3(d) display the ac magnetic susceptibility (χ'), respectively, along a and a^* axes as a function of T taken under four different frequencies. No frequency dependence is observed below 8 kHz up to 100 K, in contrast with the frequency-dependent dielectric constant (see Fig. S8 of the SM [38]). We also observed T_N and T_F, whose temperatures

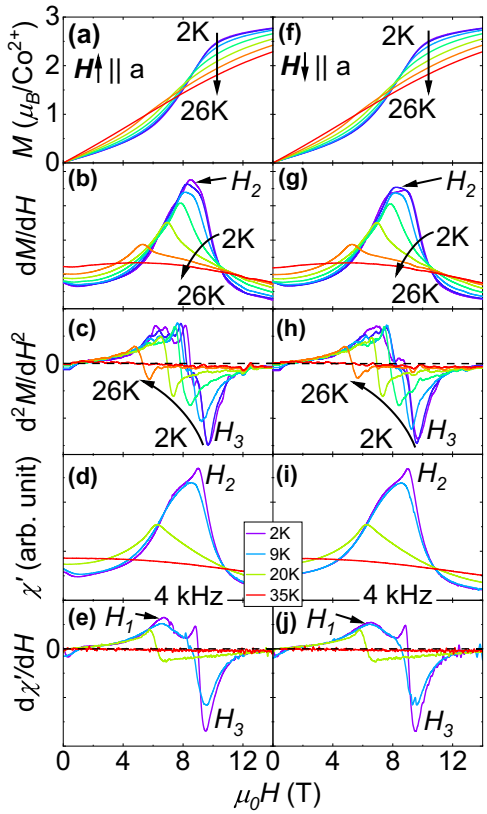

FIG. 4. dc magnetization M and ac magnetic susceptibility χ' and their first, and second derivatives with respect to magnetic field **H** as a function of **H** ∥ **a** taken in superconducting magnets. (a)–(e) display the up field sweep (**H** ↑) data in which (a)–(c) and (d), (e) are from dc and ac measurements, respectively. (f)–(j) display the down field sweep (**H** ↓) data in which (f)-(h) and (i)–(j) are from dc and ac measurements, respectively. All ac magnetic susceptibility data shown here are measured at 4 kHz. $H_{1,2,3}$ are the critical fields recorded in the phase diagram. The complete data sets are available in the SM [38].

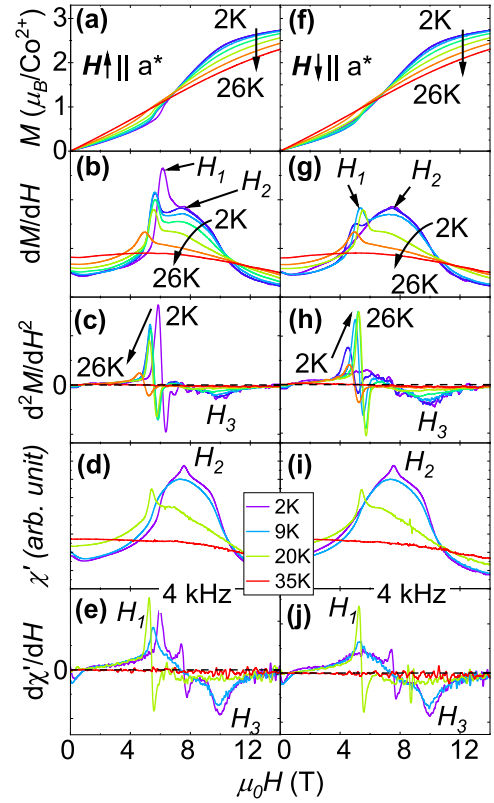

FIG. 5. dc magnetization M and ac magnetic susceptibility χ' and their first and second derivatives with respect to magnetic field **H** as a function of **H** ∥ **a** taken in superconducting magnets. (a)–(e) display the up field sweep (**H** ↑) data in which (a)–(c) and (d), (e) are from dc and ac measurements, respectively. (f)–(j) display the down field sweep (**H** ↓) data in which (f)–(h) and (i)–(j) are from dc and ac measurements, respectively. All ac magnetic susceptibility data shown here are measured at 4 kHz. $H_{1,2,3}$ are the critical fields recorded in the phase diagram. The complete data sets are available in the SM [38].

are consistent with the dc measurement while the feature of T_F is much more pronounced in ac susceptibility.

Figures 4(a)–4(c) and 4(f)–4(h) illustrate the dc magnetization [$M(H)$] at various T when **H** is applied along the a axis. Magnetization and its first and second derivatives of up (down) field sweeps are presented in Figs. 4(a)–4(c) [4(f)–4(h)], respectively. Data curves from up and down field sweeps overlap with each other, showing no hysteresis, consistent with previous reports [22,36,37]. Here we define H_2 as the inflection point of the magnetization curves found from the peak in the first derivative magnetization [Figs. 4(b) and 4(e)] and H_3 is the maximum curvature point defined as the peak in the second derivative in Figs. 4(c) and 4(h). While the H_3 phase boundary is consistent with those found in previous thermal conductivity and magnetization works [28,37], H_2 has not been called out in all previous works, despite subtle features consistently observed in previous reports [22,28,30,37]. Above H_3, the magnetization increases with a downward curvature consistent with saturation. However, a small linear component in $M(H)$ persists up to the highest measured fields of 60 T (Fig. S4), likely due to Van Vleck paramagnetism [50].

Ac magnetic susceptibility (χ') and its first derivative along the a axis are shown in Figs. 4(d), 4(e), 4(i), and 4(j) for the up and down field sweeps, respectively. All of H_1 through H_3 are observed to have similar temperature evolution compared to dc measurements. H_1 and H_3 are defined as peak and dip in the first derivative and H_2 is defined as the peak in χ'. Note that H_1 is only observed in ac measurements, likely because it is too subtle to observe in dc measurements.

Results of dc magnetization [$M(H)$] and its first and second derivatives at various T when **H** is applied along the a^* axis are shown in Figs. 5(a)–5(c) and 5(f)–5(h) for field up- and downsweeps, respectively. Three phase boundaries, H_1 through H_3, are observed in this direction. H_1 and H_2 are defined as the peak positions in the first derivative and H_3 is defined as the peak position in the second derivative of magnetization. In contrast to the a-axis data, there is noticeable hysteresis beginning at H_1 below 26 K ($\approx T_N$), as shown more clearly in Fig. S4 in the SM [38], consistent with previous reports [22,36,37]. With increasing temperature, all critical fields shift towards lower fields with peak height decreasing for both up and down field sweeps except

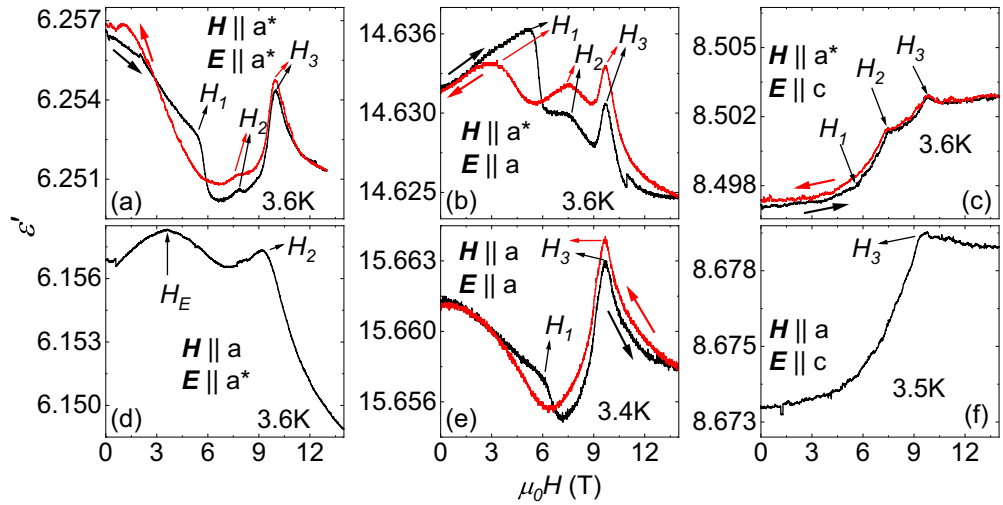

FIG. 6. Dielectric constant $\varepsilon' = \frac{\varepsilon}{\varepsilon_0}$ along all crystallographic orientations as a function of $\mathbf{H} \parallel \mathbf{a}$ [(a)–(c)] and $\mathbf{a}^*$ [(d)–(f)], taken in a superconducting magnet. Here ε is the dielectric constant of the sample and ε_0 the vacuum. $\mathbf{H} \uparrow$ and $\mathbf{H} \downarrow$ are the up and down field sweeps, respectively. $H_{1,2,3}$ are the fields recorded in the phase diagram in Fig. 2. H_1 in (c) is the kink at which the slope of the curve suddenly increases. The complete data sets are available in the SM [38].

for the H_1 peak in down sweeps whose amplitude increases with increasing temperature. Similar to the magnetization with $\mathbf{H} \parallel \mathbf{a}$, we observed the linearly increasing magnetization above the saturation magnetization because of the Van Vleck paramagnetism.

Figures 5(d), 5(e), 5(i), and 5(j) illustrate the ac susceptibility (χ') and its first derivative along the a^* axis for the up and down field sweeps, respectively. All of H_1 through H_3 are observed with similar temperature evolution compared to dc measurements. H_1 and H_3 are defined as peak and dip in the first derivative and H_2 is defined as the peak in χ'.

To check if there are no additional magnetic phase transitions, we measured the magnetization with $\mathbf{H} \parallel \mathbf{a}^*$ up to 60 T using pulsed-field magnet at 4.3 K as shown Fig. S4. The low-field section of the data agrees with dc measurements, as illustrated more clearly by dM/dH in the inset. We did not observe any additional magnetic phase transition above H_3, confirming that magnetization saturates above H_3.

Next, we investigate the electrical properties of $Na_2Co_2TeO_6$ by measuring the dielectric constant as a function of magnetic field ($\varepsilon'(H)$) for various electric and magnetic field directions as shown in Fig. 6. We note that the dielectric constant measurement has also been used to determine the phase boundaries of α-$RuCl_3$ that match well with phase boundaries obtained from other techniques [51,52]. When the magnetic field is applied along the a^* axis with electric field applied along a^*, a as shown in Figs. 6(a) and 6(b), respectively, a similar hysteresis behavior as in the magnetization measurement shown in Fig. 5 is observed. Three phase boundaries H_1, H_2, and H_3 are clearly visible as peaks in the dielectric constant, and their positions match well with those found in the magnetization. When the electric field is applied along the c axis with $\mathbf{H} \parallel \mathbf{a}^*$ [Fig. 6(c)], the peaks corresponding to H_1, H_2, and H_3 are smaller, though still sharp.

Figures 6(d)–6(f) show $\varepsilon'(H)$ for $\mathbf{H} \parallel \mathbf{a}$. An additional hump ($H_E$) is observed when electric field E is applied along the $\mathbf{a}^*$ axis. The origin of this feature needs further investigation as it does not overlap with any observations in other measurements. In contrast to the magnetization measurement, hysteretic behavior was observed for $\varepsilon'(H)$ for $\mathbf{H} \parallel \mathbf{E} \parallel \mathbf{a}$ as shown in Fig. 6(e). Since the dielectric constant strongly depends on the magnetic field and reflects the magnetic phase transition, $Na_2Co_2TeO_6$ possesses a fairly strong magnetoelectric coupling. For magnetic fields applied along the c axis, we observed negligible field dependence in the dielectric constant as shown in the SM [38].

The temperature-dependent dielectric constant and dissipation measured at various frequencies are also collected as shown in Fig. S8 of the SM [38]. The three pronounced peaks are observed in the dissipative part of the dielectric constant, whose temperatures are dependent on frequency. These do not match any feature seen in the magnetization. Considering that the dielectric constant (electric capacitance) measurement reveals the dynamics of electric dipoles, a peak/hump is expected where they undergo strong fluctuation. Therefore, a speculation is that these humps could indicate the freezing of Na^+ positions as temperature decreases. Further studies are necessary to clarify these features.

The thermodynamic properties of $Na_2Co_2TeO_6$ were also investigated and the specific heat divided by temperature (C/T) data are shown in Fig. 7 at various H up to 8.5 T. There is no significant difference between $\mathbf{H} \parallel \mathbf{a}$ and $\mathbf{a}^*$ axes. For both directions, three phase transitions are observed, consistent with our magnetization measurement and previous reports [22,37]. The T_N peak and T^* hump are observed up to 8.5 T, whereas the T_F hump is difficult to extract above 6 T. With increasing magnetic field, the peak at T_N gets weakened and suppressed to lower temperatures, whereas the T^* feature is robust against magnetic field. The T_F feature when $\mathbf{H} \parallel \mathbf{a}$ is hard to identify at several magnetic field strengths but the rest of them show a slight decreasing trend of T_F with increasing magnetic field. When $\mathbf{H} \parallel \mathbf{a}^*$, T_F is largely independent of applied magnetic field.

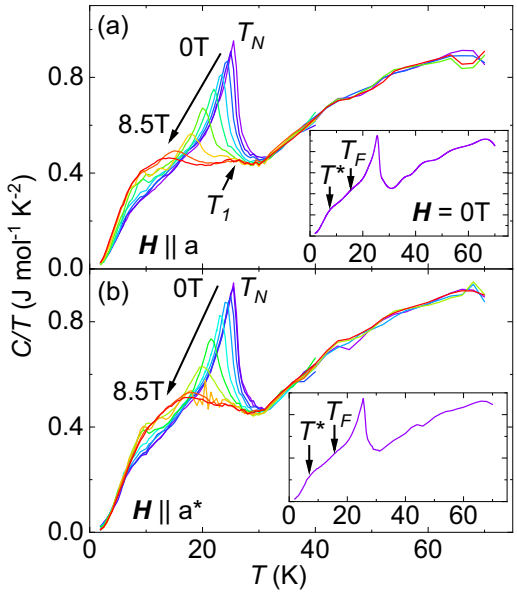

FIG. 7. Specific heat divided by temperature (C/T) as a function of T at various H up to 8.5 T for (a) $\mathbf{H} \parallel \mathbf{a}$ and (b) $\mathbf{H} \parallel \mathbf{a}^*$. The phase transition temperatures are labeled and corresponding features are indicated by the black arrows. The inset depicts the specific heat data at 0 T for a clearer view of T_F and T^*.

Figure 8 shows the magnetocaloric effect in quasiadiabatic conditions in a 65 T pulsed magnet, pulsed to a maximum field of 20 T. The sample temperature as a function of magnetic field is shown on the left axis and its derivative (dT/dH) on the right axis. The magnetic field versus time profile is shown in the inset of Fig. S14 [38]. The 20 T peak field is chosen so the fast part of the pulse occurs in the region of interest up to 12 T, and the less adiabatic behavior that emerges as the

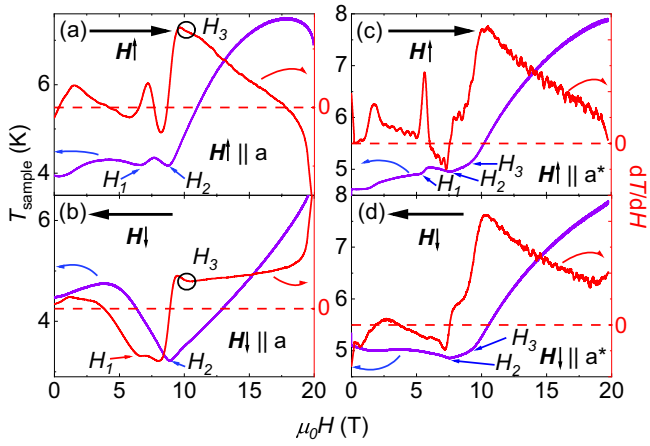

FIG. 8. Magnetocaloric effect measurements data in millisecond pulsed magnetic fields. Sample temperature T_{sample} is plotted as a function of $\mathbf{H}$ applied along both the a axis [(a), (b)] and a^* axis [(c), (d)]. The purple lines are the sample temperatures and the red lines are the derivatives ($\frac{dT}{dH}$). Phase boundaries revealed in Fig. 2 are labeled and indicated by arrows and circles. The dashed red lines are indications of $\frac{dT}{dH} = 0$. The field-sweep directions are further illustrated at the top of each plot.

sweep rate slows down and the field turns around where the sweep rate becomes zero occurs at fields above the region of interest.

We observe hysteresis in $T(H)$ originating from the first-order phase transition at H_1 that was also seen in the other properties, as well as some thermal relaxation occurring at the highest fields where the field-sweep rate slows down and passes through zero, causing the adiabatic behavior to become quasiadiabatic. We note that with increasing field-sweep speed, the hysteresis of first-order phase transitions generally broadens due to the finite time needed to nucleate and grow the new phase. Thus, the hysteresis in H_1 can be expected to open significantly in these pulsed measurements. In some cases, first-order phase transitions can be avoided altogether at fast sweep rates due to lack of time for the new phase to nucleate and grow (supercooling/superfielding). On the other hand, the nonhysteretic second-order-like phase transitions at H_2 and H_3 can be observed at similar fields as in dc magnetization measurements.

In the $T(H)$ data in Fig. 8, we indicate the phase transitions H_1, H_2, and H_3 with arrows. These phase transitions appear as minima. This is consistent with increased spin disorder when approaching a phase transition, which forces the thermal entropy to drop to compensate. When $\mathbf{H} \parallel \mathbf{a}$, H_3 is difficult to observe due to a large background increase in temperature approaching saturation but can be resolved as a wiggle in dT/dH. These observations are similar to those made for magnetocaloric effect data in α-$RuCl_3$ [53,54]. Above H_3, the temperature increases rapidly. This temperature increase reflects the spin gap that opens above magnetic saturation [28]. The increase in thermal entropy compensates for the drop in spin entropy as the magnetization saturates and a spin gap opens and increases with increasing magnetic field.

When the magnetic field is parallel with a^*, all three phase boundaries are clearly resolved in $T(H)$ as well as dT/dH on the upsweep. We miss seeing H_1 in the down field sweep as described above. All of H_1, H_2, and H_3 are observed as dips and kinks in the $T(H)$ curve or its first derivative.

We now move to thermal expansion and magnetostriction, i.e., length changes of the sample with temperature and field. Shown in Fig. 9 are the thermal expansion data of $Na_2Co_2TeO_6$ as a function of T with $\mathbf{H} \parallel \mathbf{a}$ and $\mathbf{a}^*$ up to 14 T. Unlike α-$RuCl_3$ [54], along both a and a^* axes, the thermal expansion $[\Delta a(a^*)/a_0(a_0^*)]$ shows very little temperature dependence at zero magnetic field, consistent with previous studies showing no structural transition [27,31,47]. However, with increasing field, along the a axis, a kink at T_1 develops, indicating an onset of slope change. This becomes more and more pronounced with increasing field until 6 T, above which the shape of the thermal expansion *abruptly* changes and a sharp drop appears at T_2. At even higher fields, the T_2 feature broadens and eventually becomes a gradual decrease. Both features are observed almost always outside the antiferromagnetic phase of $Na_2Co_2TeO_6$ and are independent of magnetic field strength, as illustrated in Fig. 2. The origin of T_1 and T_2 are not yet determined and need further experimental input from structural-sensitive measurements such as x-ray or neutron diffraction. On the other hand, along the a^* axis, all features are broad and we do not identify any phase transitions.

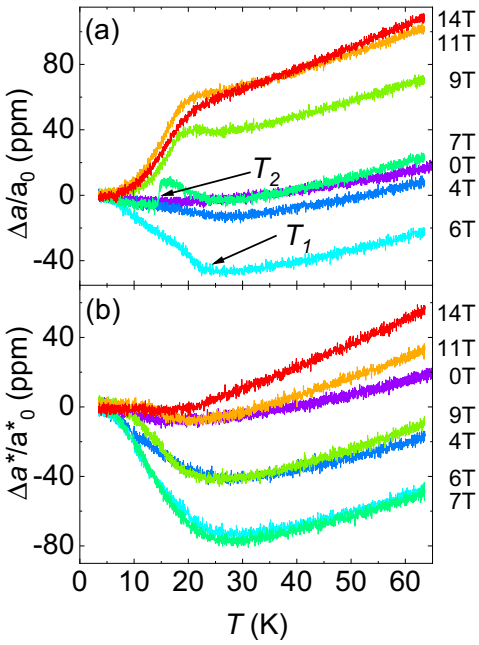

FIG. 9. Thermal expansion as a function of temperature T in (a) a axis ($\Delta a/a_0$) and (b) a^* axis ($\Delta a^*/a_0^*$) with various magnetic fields **H** applied along the same direction as the length change. $T_{1,2}$ represent the phase boundaries/crossovers recorded in the phase diagram. All data curves are normalized to the corresponding lowest-temperature thermal expansion values. The complete data sets are available in the SM [38].

The magnetostriction data are shown in Fig. 10. When **H** ∥ **a**, a peak is observed in the magnetostriction at 6–7 T, corresponding to H_1, followed by a discontinuous and hysteretic jump at H_{first}. In the upsweeps, the amplitude of this jump decreases with increasing temperature until T_F, above which it disappears. But in the downsweeps, the amplitude of this

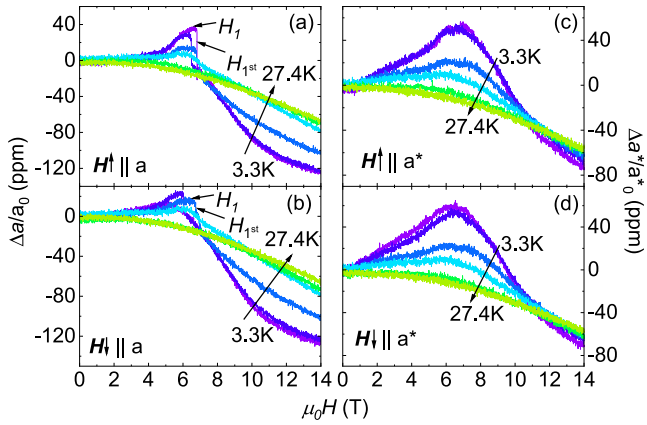

FIG. 10. Magnetostriction as a function of applied magnetic field **H** in a superconducting magnet taken at various temperatures as indicated for both the a axis [(a), (b)] and a^* axis [(c), (d)]. **H** ↑ and **H** ↓ are the up and down field sweeps, respectively. H_0 and H_{first} are the phase boundaries/crossovers recorded in the phase diagram. All data curves are normalized to the corresponding zero field thermal expansion values. The complete data sets are available in the SM [38].

drop feature increases with increasing T until T_F at which the up- and downsweep curves overlap with each other. It then suddenly becomes much weaker at higher temperatures and eventually becomes invisible above 22 K. On the other hand, along the a^* axis, only a broad maximum is observed which does not correspond to any phase transitions.

B. Discussion

Magnetic field versus temperature phase diagrams were built by combining the data from the Results subsection. In Fig. 2, we show the phase diagrams for the magnetic field in the plane. The four phase diagram correspond to up and down field sweeps for **H** ∥ **a** and **a***. (In the SM [38] we also show the phase diagram for **H** ∥ **c**.)

The phase diagrams in Fig. 2 show four phases as a function of magnetic field. These phases are denoted as I–IV, in addition to the high-temperature paramagnetic phase. These four phases contrast with some of the previous studies where only three phases were observed [22,29], probably due to the limited number of measured quantities or field range in those studies. Recently, a study of torque magnetometry and inelastic neutron scattering also showed some evidence of all four phases [30].

For **H** ∥ **a**, we also observe apparent phase transitions T_1 and T_2 as a function of temperature in the thermal expansion and specific heat at high fields that were not previous reported.

Our comprehensive phase diagrams reveal a couple of interesting features of those phases. First, the phase boundaries H_1 and H_2 are nearly independent of temperature. Successive temperature-independent phase boundaries are not often observed except for in frustrated magnets [54–58]. Therefore, this observation supports the existence of magnetic frustration in $Na_2Co_2TeO_6$, which is expected from Kitaev interactions as well as off-diagonal symmetric anisotropy, Γ terms [59,60]. Among these phase transitions, the H_1 boundary along the a^* axis is clearly first order, showing hysteresis between up and down field sweeps and metamagnetic behavior with a sudden change in magnetization (Fig. 5). Along the a axis, we find that H_1 involves a rather large and discontinuous lattice distortion, as illustrated in the magnetostriction measurement. Considering that the spins are aligned along the a axis in $Na_2Co_2TeO_6$ [27], this is different from a simple spin-flop or spin-flip phase transitions.

Recent inelastic neutron scattering and thermal conductivity measurements [28,30] suggest that the phase between H_2 and H_3 could possibly be a KQSL phase. It shows a restoration to an approximately sixfold symmetry in the hexagonal plane and a broad region of low-lying excitations. Further studies are needed to distinguish KQSL from disordered or other possible phases.

We start by discussing the properties of the low-temperature, low-field phase I. The zero-field magnetic long-range ordering occurs below 27 K (T_N) and two subsequent phase transitions at 15 K (T_F) and 5 K (T^*) are observed, consistent with other literature, and therein their natures are discussed [22,29]. When the magnetic field is applied along the a axis in phase I, the first-order H_1 phase transition to likely another antiferromagnetic phase (phase II) is clearly revealed in ac magnetic susceptibility (Fig. 4), dielectric constant (Fig. 6), magnetocaloric effect (Fig. 8),

and magnetostriction (Fig. 10) in upsweeps. The transition involves a strong lattice contraction along the a axis. Similar behaviors in ac magnetic susceptibility, thermal conductivity, magnetostriction, and magnetocaloric effect have been observed in α-$RuCl_3$ [54,61,62].

Moving on to $\mathbf{H} \parallel \mathbf{a}^*$ for H_1, the phase boundary is observed in dc magnetization and ac magnetic susceptibility both with a hysteresis loop (Fig. 5, S5 in the SM [38]), dielectric constant (Fig. 6), and magnetocaloric effect measurements (Fig. 8). One obvious difference compared to $\mathbf{H} \parallel \mathbf{a}$ is that for $\mathbf{H} \parallel \mathbf{a}^*$, the H_1 feature is more pronounced in dc magnetization $\mathbf{a}^*$ measurements. This is not unreasonable as antiferromagnetic transitions are not always revealed in magnetization measurements. Another noticeable difference between a and a^* axes is from the dielectric constant. H_1 is observed regardless of electric field directions when $\mathbf{H} \parallel \mathbf{a}^*$ but only with $\mathbf{E} \parallel \mathbf{a}$ when $\mathbf{H} \parallel \mathbf{a}$. We note that phase II has different lattice constants from the zigzag antiferromagnetic ground state due to the first-order phase transition at H_1. Further investigation such as neutron diffraction and x-ray measurements in magnetic field are necessary to investigate this.

The H_2 phase boundary is similar for $\mathbf{H} \parallel \mathbf{a}$ and $\mathbf{a}^*$ directions. It is observed in dc magnetization, ac susceptibility (Figs. 4 and 5), dielectric constant (Fig. 6), and magnetocaloric effect (Fig. 8) measurements. It manifests as a dip ($\mathbf{H} \parallel \mathbf{a}$) or a kink ($\mathbf{H} \parallel \mathbf{a}^*$) in $T(H)$ curves where the sample temperature starts to increase monotonically with increasing field. Such increase in lattice entropy in turn indicates a decrease in spin entropy in phase III under an quasi-adiabatic condition. Phase III has been proposed recently as a candidate KQSL phase according to the apparent resumption of the hexagonal symmetry in magnetic torque measurements, inelastic neutron diffraction measurements [30], and low-lying magnetic excitations in thermal conductivity [28]. It is counterintuitive that the spin entropy would decrease upon entering a spin liquid phase. However, we note that two types of KQSL phases exist: one is gapless and the other is gapped [63]. For the former, gapless excitations contribute to the spin entropy at finite temperatures and, thus, sample temperature would decrease within this phase. For the latter, energy gap protects the ground state and the spin entropy would decrease within this phase. Hence an increase of sample temperature is expected. Therefore, assuming phase III is indeed a KQSL phase, our results are more consistent with gapped KQSL scenario. In addition, we note that for KQSL-candidate α-$RuCl_3$ the same entropy decrease was observed [54].

As reported in the literature [28,37], the H_3 phase boundary appears like a continuation of the T_N boundary from magnetization and specific heat measurements, with a mean-field-like shape in field temperature. However, this phase boundary encompasses multiple magnetic phases I–III. Note that when $\mathbf{H} \parallel \mathbf{a}$, H_3 is only clearly observed in dc magnetization, ac magnetic susceptibility, and dielectric constant measurements, but for $\mathbf{H} \parallel \mathbf{a}^*$, its feature is also very pronounced in the magnetocaloric effect.

Above H_3, the dc magnetization versus magnetic field becomes convex, appearing to saturate, as explained in the previous section. The sample temperature from the magnetocaloric effect continuously increases, consistent with a spin gap opening with increasing magnetic field. These two features support that phase IV is the spin-polarized phase, albeit with a magnetization that continues to slightly increase linearly up to at least 60 T due to a Van Vleck effect. A peak in the dielectric constant is usually associated with a phase transition involving electric dipole moments. As our electric polarization measurement did not yield any net electric polarization in this compound, such an electric ordering would have to be an antiferroelectric or disordered arrangement. The idea that Majorana excitations out of the KQSL phase create electrical patterns has been proposed for α-$RuCl_3$, though there the electric patterns have no net dipole as they are radially symmetric [64]. In general, magnetic spin configurations are known to produce electric polarization when the magnetism in conjunction with the lattice creates a polar axis or, alternatively, magnetic configurations can create local dipoles that cancel each other in the bulk preventing a net electric polarization. Here, studying the possibility that a putative KQSL phase or its excitations could carry electric dipoles in $Na_2Co_2TeO_6$ will be an interesting future work.

Finally, we note that for $\mathbf{H} \parallel \mathbf{a}^*$ there is an apparent tricritical point where T_N, H_2, and H_3 meet. If these are all second-order phase transitions, such a tricritical point is not allowed by symmetry [65] or free-energy continuity arguments [66]. One possibility is that one of these phase boundaries is not a second-order phase transition. Another possibility is that this tricritical point merges with the first-order H_1 phase boundary, though this is not fully supported by our data. For $\mathbf{H} \parallel \mathbf{a}$, there is no observed tricritical point of second-order phase transitions due to the addition of the T_2 phase line. We note also that where T_1 joins T_N, there may be a tricritical point, but more likely T_1 joins T_N at $H = 0$, removing that conundrum.

V. CONCLUSION

In this paper, we established a comprehensive $T - \mathbf{H}$ phase diagram of $Na_2Co_2TeO_6$ based on its magnetic, electric, thermodynamic, and elastic properties. Three successive field-induced magnetic phases (I–III) are observed before magnetic saturation (IV), and the phase boundaries (H_1, H_2) are largely independent of temperature. This suggests the existence of magnetic frustration. Moreover, the dielectric constant is heavily dependent on magnetic field and it reveals all of the magnetic phase transitions, indicating a strong magnetoelectric coupling in $Na_2Co_2TeO_6$ though without a measurable net electric polarization. Of the two proposed spin structures for phase I at zero magnetic field, the zigzag state fits our data better. By symmetry, the zigzag state should not show an electric polarization in zero or applied magnetic fields, consistent with our measurements. The microscopic nature of phase II and III are still under investigation. But our paper indicates that phase II has different lattice constants compared to those in phase I, and phase III has lower spin entropy than phase II. At even higher fields, $Na_2Co_2TeO_6$ enters the spin-polarized phase (IV) where a spin gap opens. Strong peaks in the dielectric constant at the boundary between phase III and phase IV are consistent with an antiferroelectric or disordered-electric phase transition in conjunction with the magnetic one.

ACKNOWLEDGMENTS

We acknowledge M. Jamie for valuable discussions. This work was principally lead by and supported by the U.S. Department of Energy, Office of Science, National Quantum Information Sciences Research Centers, Quantum Science Center. The facilities of the National High Magnetic Field Laboratory are supported by the National Science Foundation Cooperative Agreement No. DMR-1644779, and the State of Florida and the U.S. Department of Energy. Q.H. and H.D.Z. grew the samples with support from the National Science Foundation Grant No. DMR-2003117. M.L. and S.M.T. acknowledge the LDRD program at Los Alamos National Laboratory for some initial work they did before joining the Quantum Science Center. W.K.P. acknowledges support from the G. T. Seaborg Institute Postdoctoral Fellow Program.

[1] A. Kitaev, Anyons in an exactly solved model and beyond, Ann. Phys. **321**, 2 (2006).

[2] C. Nayak, S. H. Simon, A. Stern, M. Freedman, and S. Das Sarma, Non-Abelian anyons and topological quantum computation, Rev. Mod. Phys. **80**, 1083 (2008).

[3] Y. Kasahara, T. Ohnishi, Y. Mizukami, O. Tanaka, S. Ma, K. Sugii, N. Kurita, H. Tanaka, J. Nasu, Y. Motome, T. Shibauchi, and Y. Matsuda, Majorana quantization and half-integer thermal quantum Hall effect in a Kitaev spin liquid, Nature (London) **559**, 227 (2018).

[4] Y. Kasahara, S. Suetsugu, T. Asaba, S. Kasahara, T. Shibauchi, N. Kurita, H. Tanaka, and Y. Matsuda, Quantized and unquantized thermal Hall conductance of the Kitaev spin liquid candidate α-$RuCl_3$, Phys. Rev. B **106**, L060410 (2022).

[5] G. Jackeli and G. Khaliullin, Mott Insulators in the Strong Spin-Orbit Coupling Limit: From Heisenberg to a Quantum Compass and Kitaev Models, Phys. Rev. Lett. **102**, 017205 (2009).

[6] J. Chaloupka, G. Jackeli, and G. Khaliullin, Kitaev-Heisenberg Model on a Honeycomb Lattice: Possible Exotic Phases in Iridium Oxides A_2IrO_3, Phys. Rev. Lett. **105**, 027204 (2010).

[7] K. Kitagawa, T. Takayama, Y. Matsumoto, A. Kato, R. Takano, Y. Kishimoto, S. Bette, R. Dinnebier, G. Jackeli, and H. Takagi, A spin–orbital-entangled quantum liquid on a honeycomb lattice, Nature (London) **554**, 341 (2018).

[8] F. Bahrami, W. Lafargue-Dit-Hauret, O. I. Lebedev, R. Movshovich, H.-Y. Yang, D. Broido, X. Rocquefelte, and F. Tafti, Thermodynamic Evidence of Proximity to a Kitaev Spin Liquid in $Ag_3LiIr_2O_6$, Phys. Rev. Lett. **123**, 237203 (2019).

[9] A. Chakraborty, V. Kumar, S. Bachhar, N. Büttgen, K. Yokoyama, P. K. Biswas, V. Siruguri, S. Pujari, I. Dasgupta, and A. V. Mahajan, Unusual spin dynamics in the low-temperature magnetically ordered state of $Ag_3LiIr_2O_6$, Phys. Rev. B **104**, 115106 (2021).

[10] F. Bahrami, E. M. Kenney, C. Wang, A. Berlie, O. I. Lebedev, M. J. Graf, and F. Tafti, Effect of structural disorder on the Kitaev magnet $Ag_3LiIr_2O_6$, Phys. Rev. B **103**, 094427 (2021).

[11] Y. Li and R. Valentí, Role of disorder in electronic and magnetic properties of $Ag_3LiIr_2O_6$, Phys. Rev. B **105**, 115123 (2022).

[12] K. W. Plumb, J. P. Clancy, L. J. Sandilands, V. V. Shankar, Y. F. Hu, K. S. Burch, H.-Y. Kee, and Y.-J. Kim, α- $RuCl_3$: A spin-orbit assisted Mott insulator on a honeycomb lattice, Phys. Rev. B **90**, 041112(R) (2014).

[13] A. Banerjee, C. Bridges, J.-Q. Yan, A. Aczel, L. Li, M. Stone, G. Granroth, M. Lumsden, Y. Yiu, J. Knolle *et al.*, Proximate Kitaev quantum spin liquid behaviour in a honeycomb magnet, Nat. Mater. **15**, 733 (2016).

[14] S.-H. Do, S.-Y. Park, J. Yoshitake, J. Nasu, Y. Motome, Y. S. Kwon, D. T. Adroja, D. J. Voneshen, K. Kim, T.-H. Jang, J.-H. Park, K.-Y. Choi, and S. Ji, Majorana fermions in the Kitaev quantum spin system α-$RuCl_3$, Nat. Phys. **13**, 1079 (2017).

[15] P. Czajka, T. Gao, M. Hirschberger, P. Lampen-Kelley, A. Banerjee, J. Yan, D. G. Mandrus, S. E. Nagler, and N. Ong, Oscillations of the thermal conductivity in the spin-liquid state of α-$RuCl_3$, Nat. Phys. **17**, 915 (2021).

[16] J. Bruin, R. Claus, Y. Matsumoto, J. Nuss, S. Laha, B. Lotsch, N. Kurita, H. Tanaka, and H. Takagi, Origin of oscillatory structures in the magnetothermal conductivity of the putative Kitaev magnet α-$RuCl_3$, APL Mater. **10**, 090703 (2022).

[17] J. Bruin, R. Claus, Y. Matsumoto, N. Kurita, H. Tanaka, and H. Takagi, Robustness of the thermal Hall effect close to half-quantization in α-$RuCl_3$, Nat. Phys. **18**, 401 (2022).

[18] H. Liu and G. Khaliullin, Pseudospin exchange interactions in d^7 cobalt compounds: possible realization of the Kitaev model, Phys. Rev. B **97**, 014407 (2018).

[19] R. Sano, Y. Kato, and Y. Motome, Kitaev-Heisenberg Hamiltonian for high-spin d^7 Mott insulators, Phys. Rev. B **97**, 014408 (2018).

[20] H. Liu, Towards Kitaev spin liquid in 3d transition metal compounds, Int. J. Mod. Phys. B **35**, 2130006 (2021).

[21] C. Kim, J. Jeong, G. Lin, P. Park, T. Masuda, S. Asai, S. Itoh, H.-S. Kim, H. Zhou, J. Ma *et al.*, Antiferromagnetic Kitaev interaction in $J_{eff} = 1/2$ cobalt honeycomb materials $Na_3Co_2SbO_6$ and $Na_2Co_2TeO_6$, J. Phys.: Condens. Matter **34**, 045802 (2022).

[22] G. Lin, J. Jeong, C. Kim, Y. Wang, Q. Huang, T. Masuda, S. Asai, S. Itoh, G. Günther, M. Russina *et al.*, Field-induced quantum spin disordered state in spin-1/2 honeycomb magnet $Na_2Co_2TeO_6$, Nat. Commun. **12**, 5559 (2021).

[23] A. L. Sanders, R. A. Mole, J. Liu, A. J. Brown, D. Yu, C. D. Ling, and S. Rachel, Dominant Kitaev interactions in the honeycomb materials $Na_3Co_2SbO_6$ and $Na_2Co_2TeO_6$, Phys. Rev. B **106**, 014413 (2022).

[24] W. Yao, K. Iida, K. Kamazawa, and Y. Li, Excitations in the Ordered and Paramagnetic States of Honeycomb Magnet $Na_2Co_2TeO_6$, Phys. Rev. Lett. **129**, 147202 (2022).

[25] L. Viciu, Q. Huang, E. Morosan, H. Zandbergen, N. Greenbaum, T. McQueen, and R. Cava, Structure and basic magnetic properties of the honeycomb lattice compounds $Na_2Co_2TeO_6$ and $Na_3Co_2SbO_6$, J. Solid State Chem. **180**, 1060 (2007).

[26] S. M. Winter, Magnetic couplings in edge-sharing high-spin d^7 compounds, J. Phys. Mater. **5**, 045003 (2022).

[27] A. K. Bera, S. M. Yusuf, A. Kumar, and C. Ritter, Zigzag antiferromagnetic ground state with anisotropic correlation lengths in the quasi-two-dimensional honeycomb lattice compound $Na_2Co_2TeO_6$, Phys. Rev. B **95**, 094424 (2017).

[28] X. Hong, M. Gillig, R. Hentrich, W. Yao, V. Kocsis, A. R. Witte, T. Schreiner, D. Baumann, N. Pérez, A. U. B. Wolter, Y. Li, B. Buchner, and C. Hess, Strongly scattered phonon heat transport of the candidate Kitaev material $Na_2Co_2TeO_6$, Phys. Rev. B **104**, 144426 (2021).

[29] G. Xiao, Z. Xia, Y. Song, and L. Xiao, Magnetic properties and phase diagram of quasi-two-dimensional $Na_2Co_2TeO_6$ single crystal under high magnetic field, J. Phys.: Condens. Matter **34**, 075801 (2022).

[30] G. Lin, Q. Zhao, G. Li, M. Shu, Y. Ma, J. Jiao, Q. Huang, J. Sheng, A. Kolesnikov, L. Li *et al.*, Evidence for field induced quantum spin liquid behavior in a spin-1/2 honeycomb magnet, Research Square (2022), https://doi.org/10.21203/rs.3.rs-2034295/v1.

[31] E. Lefrançois, M. Songvilay, J. Robert, G. Nataf, E. Jordan, L. Chaix, C. V. Colin, P. Lejay, A. Hadj-Azzem, R. Ballou *et al.*, Magnetic properties of the honeycomb oxide $Na_2Co_2TeO_6$, Phys. Rev. B **94**, 214416 (2016).

[32] R. D. Johnson, S. C. Williams, A. A. Haghighirad, J. Singleton, V. Zapf, P. Manuel, I. I. Mazin, Y. Li, H. O. Jeschke, R. Valentí, and R. Coldea, Monoclinic crystal structure of α-$RuCl_3$ and the zigzag antiferromagnetic ground state, Phys. Rev. B **92**, 235119 (2015).

[33] M. Songvilay, J. Robert, S. Petit, J. A. Rodriguez-Rivera, W. D. Ratcliff, F. Damay, V. Balédent, M. Jiménez-Ruiz, P. Lejay, E. Pachoud, A. Hadj-Azzem, V. Simonet, and C. Stock, Kitaev interactions in the Co honeycomb antiferromagnets $Na_3Co_2SbO_6$ and $Na_2Co_2TeO_6$, Phys. Rev. B **102**, 224429 (2020).

[34] A. M. Samarakoon, Q. Chen, H. Zhou, and V. O. Garlea, Static and dynamic magnetic properties of honeycomb lattice antiferromagnets $Na_2M_2TeO_6$, M = Co and Ni, Phys. Rev. B **104**, 184415 (2021).

[35] W. Chen, X. Li, Z. Hu, Z. Hu, L. Yue, R. Sutarto, F. He, K. Iida, K. Kamazawa, W. Yu *et al.*, Spin-orbit phase behavior of $Na_2Co_2TeO_6$ at low temperatures, Phys. Rev. B **103**, L180404 (2021).

[36] C. H. Lee, S. Lee, Y. S. Choi, Z. H. Jang, R. Kalaivanan, R. Sankar, and K.-Y. Choi, Multistage development of anisotropic magnetic correlations in the Co-based honeycomb lattice $Na_2Co_2TeO_6$, Phys. Rev. B **103**, 214447 (2021).

[37] W. Yao and Y. Li, Ferrimagnetism and anisotropic phase tunability by magnetic fields in $Na_2Co_2TeO_6$, Phys. Rev. B **101**, 085120 (2020).

[38] See Supplemental Material at http://link.aps.org/supplemental/10.1103/PhysRevB.108.064421 for electronic and magnetic phase diagrams of Kitaev quantum spin liquid candidate $Na_2Co_2TeO_6$.

[39] V. S. Zapf, M. Kenzelmann, F. Wolff-Fabris, F. Balakirev, and Y. Chen, Magnetically induced electric polarization in an organometallic magnet, Phys. Rev. B **82**, 060402(R) (2010).

[40] Y.-S. Chai, J.-Z. Cong, J.-C. He, D. Su, X.-X. Ding, J. Singleton, V. Zapf, and Y. Sun, Giant magnetostriction and nonsaturating electric polarization up to 60 T in the polar magnet $CaBaCo_4O_7$, Phys. Rev. B **103**, 174433 (2021).

[41] M. Jaime, C. Corvalán Moya, F. Weickert, V. Zapf, F. F. Balakirev, M. Wartenbe, P. F. Rosa, J. B. Betts, G. Rodriguez, S. A. Crooker *et al.*, Fiber Bragg grating dilatometry in extreme magnetic field and cryogenic conditions, Sensors **17**, 2572 (2017).

[42] M. Fiebig, Revival of the magnetoelectric effect, J. Phys. D **38**, R123 (2005).

[43] A. Agyei and J. L. Birman, On the linear magnetoelectric effect, J. Phys.: Condens. Matter **2**, 3007 (1990).

[44] J.-P. Rivera, The linear magnetoelectric effect in $LiCoPO_4$ revisited, Ferroelectrics **161**, 147 (1994).

[45] N. A. Spaldin and R. Ramesh, Advances in magnetoelectric multiferroics, Nat. Mater. **18**, 203 (2019).

[46] S. Mukherjee, G. Manna, P. Saha, S. Majumdar, and S. Giri, Ferroelectric order with a linear high-field magnetoelectric coupling in $Na_2Co_2TeO_6$: A proposed Kitaev compound, Phys. Rev. Mater. **6**, 054407 (2022).

[47] G. Xiao, Z. Xia, W. Zhang, X. Yue, S. Huang, X. Zhang, F. Yang, Y. Song, M. Wei, H. Deng *et al.*, Crystal growth and the magnetic properties of $Na_2Co_2TeO_6$ with quasi-two-dimensional honeycomb lattice, Cryst. Growth Des. **19**, 2658 (2019).

[48] N. A. Spaldin, M. Fiebig, and M. Mostovoy, The toroidal moment in condensed-matter physics and its relation to the magnetoelectric effect, J. Phys.: Condens. Matter **20**, 434203 (2008).

[49] W. Yao, Y. Zhao, Y. Qiu, C. Balz, J. R. Stewart, J. W. Lynn, and Y. Li, Magnetic ground state of the Kitaev $Na_2Co_2TeO_6$ spin liquid candidate, Phys. Rev. Res. **5**, L022045 (2023).

[50] M. Lee, J. Hwang, E. S. Choi, J. Ma, C. R. Dela Cruz, M. Zhu, X. Ke, Z. L. Dun, and H. D. Zhou, Series of phase transitions and multiferroicity in the quasi-two-dimensional spin-$\frac{1}{2}$ triangular-lattice antiferromagnet $Ba_3CoNb_2O_9$, Phys. Rev. B **89**, 104420 (2014).

[51] X. Mi, X. Wang, H. Gui, M. Pi, T. Zheng, K. Yang, Y. Gan, P. Wang, A. Li, A. Wang *et al.*, Stacking faults in α-$RuCl_3$ revealed by local electric polarization, Phys. Rev. B **103**, 174413 (2021).

[52] J.-C. Zheng, Y. Cui, T.-R. Li, K.-J. Ran, J. Wen, and W. Yu, Dielectric evidence for possible type-II multiferroicity in α-$RuCl_3$, Sci. China Phys. Mech. Astron. **61**, 057021 (2018).

[53] S. Bachus, D. A. S. Kaib, Y. Tokiwa, A. Jesche, V. Tsurkan, A. Loidl, S. M. Winter, A. A. Tsirlin, R. Valenti, and P. Gegenwart, Thermodynamic Perspective on Field-Induced Behavior of α-$RuCl_3$, Phys. Rev. Lett. **125**, 097203 (2020).

[54] R. Schönemann, S. Imajo, F. Weickert, J. Yan, D. G. Mandrus, Y. Takano, E. L. Brosha, P. F. S. Rosa, S. E. Nagler, K. Kindo, and M. Jaime, Thermal and magnetoelastic properties of α- $RuCl_3$ in the field-induced low-temperature states, Phys. Rev. B **102**, 214432 (2020).

[55] M. Lee, E. S. Choi, X. Huang, J. Ma, C. R. Dela Cruz, M. Matsuda, W. Tian, Z. L. Dun, S. Dong, and H. D. Zhou, Magnetic phase diagram and multiferroicity of $Ba_3MnNb_2O_9$: A spin-$\frac{5}{2}$ triangular lattice antiferromagnet with weak easy-axis anisotropy, Phys. Rev. B **90**, 224402 (2014).

[56] J. A. Sears, Y. Zhao, Z. Xu, J. W. Lynn, and Y.-J. Kim, Phase diagram of α-$RuCl_3$ in an in-plane magnetic field, Phys. Rev. B **95**, 180411(R) (2017).

[57] Q. Huang, M. Lee, E. S. Choi, J. Ma, C. D. Cruz, and H. D. Zhou, Successive phase transitions and multiferroicity in deformed triangular-lattice antiferromagnets $Ca_3MNb_2O_9$ (M = Co, Ni) with spatial anisotropy, ECS J. Solid State Sci. Technol. **11**, 063004 (2022).

[58] G.-W. Chern, Y. Sizyuk, C. Price, and N. B. Perkins, Kitaev-Heisenberg model in a magnetic field: Order-by-disorder and

commensurate-incommensurate transitions, Phys. Rev. B **95**, 144427 (2017).

[59] L. Janssen, E. C. Andrade, and M. Vojta, Honeycomb-Lattice Heisenberg-Kitaev Model in a Magnetic Field: Spin Canting, Metamagnetism, and Vortex Crystals, Phys. Rev. Lett. **117**, 277202 (2016).

[60] L. Janssen and M. Vojta, Heisenberg-Kitaev physics in magnetic fields, J. Phys.: Condens. Matter **31**, 423002 (2019).

[61] C. Balz, P. Lampen-Kelley, A. Banerjee, J. Yan, Z. Lu, X. Hu, S. M. Yadav, Y. Takano, Y. Liu, D. A. Tennant, M. D. Lumsden, D. Mandrus, and S. E. Nagler, Finite field regime for a quantum spin liquid in α-$RuCl_3$, Phys. Rev. B **100**, 060405(R) (2019).

[62] C. Balz, L. Janssen, P. Lampen-Kelley, A. Banerjee, Y. H. Liu, J.-Q. Yan, D. G. Mandrus, M. Vojta, and S. E. Nagler, Field-induced intermediate ordered phase and anisotropic interlayer interactions in α-$RuCl_3$, Phys. Rev. B **103**, 174417 (2021).

[63] S. Trebst and C. Hickey, Kitaev materials, Phys. Rep. **950**, 1 (2022).

[64] R. G. Pereira and R. Egger, Electrical Access to Ising Anyons in Kitaev Spin Liquids, Phys. Rev. Lett. **125**, 227202 (2020).

[65] L. D. Landau, Zh. Eksp. Teor. Fiz. **7**, 627 (1937); On the theory of phase transitions, in *Collected Papers of L.D. Landau*, edited by D. Ter Haar (Pergamon Press, Oxford, UK, 1965), Chap. 29, pp. 193–216.

[66] S. K. Yip, T. Li, and P. Kumar, Thermodynamic considerations and the phase diagram of superconducting UPt_3, Phys. Rev. B **43**, 2742 (1991).